

# Mechanical properties of magnesium-based wood-like material subjected to splitting tensile tests

Chunjie Li <sup>a,b</sup>, Hongniao Chen <sup>a,b,\*</sup>, Huagang Zhang <sup>a,b</sup>, T. James Marrow <sup>c,\*\*</sup>

<sup>a</sup> Research Center of Space Structures, Guizhou University, Guiyang 550025, China

<sup>b</sup> Key Laboratory of Structural Engineering of Guizhou Province, Guiyang 550025, China

<sup>c</sup> Department of Materials, Oxford University, Parks Road, Oxford OX1 3PH, United Kingdom

## ARTICLE INFO

### Keywords:

Magnesium-based wood-like material

DIC

Splitting tensile tests

Crack modes

The elastic Young modulus

## ABSTRACT

To investigate the splitting tensile characteristics of a new building material, namely magnesium-based wood-like material (MWM), the cubic splitting tensile tests were carried out at a loading rate of 200 N/s. Full-field displacements and crack behaviors were measured using Digital Image Correlation, and the splitting tensile strength is 1.79 MPa. The elastic Young modulus, Poisson's ratio, and axial compressive strength were measured as 2.21 GPa, 0.21, 8.76 MPa respectively. In the splitting tensile tests, primary cracks were observed to initiate from the geometric centre of the specimen and then extend to the loading ends where secondary cracks appeared. A new method for identifying cracking modes showed the secondary cracks were mainly caused by shear and tensile-shear failure, whereas the primary cracks were caused by tensile failure. An accurate method for estimating the elastic Young modulus, simultaneously with the determination of the splitting tensile strength of MWM cubes is proposed.

## 1. Introduction

At present, the annual production of straw in China exceeds 900 million tons and global annual production has reached nearly 3.8 billion tons, with most straw burned or discarded [1,2]. Burning straw has caused serious environmental pollution, especially increased haze. To support the trend for environmental protection and low-carbon development and promote the utilization of straw, it is necessary to understand the mechanical properties of materials manufactured from straw [3]. The use of straw fibres in modern construction materials has become popular and could play an important role in energy saving [4]. Ding et al. [5] proposed that adding straw fibres to cementitious materials could improve mechanical properties and reduce the density. Niu et al. [4] took corn straws as raw materials to prepare a cementitious composite material with the aim of solving the problem of high energy consumption in rural housing. Additionally sawdust, as a by-product of wood processing, is both an environmental pollutant and a potential fire hazard and may also cause respiratory problems, thus recycling of sawdust into construction materials not only meets an urgent need but also addresses environmental and healthy problems [6,7]. To this end, Raheem et al. [8] established a method to partially replace ordinary silicate cement clinker with sawdust in cement production, but Charles et al. [9] found that sawdust was not fully compatible with alkaline silicate cement. To solve this problem, Andreea et al. [10] proposed using magnesium-based cement.

Magnesium Oxychloride Cement (MOC) has advantageous high strength, fast hardening, low density, good thermal insulation and

\* Corresponding author at: Research Center of Space Structures, Guizhou University, Guiyang 550025, China.

\*\* Corresponding author.

E-mail addresses: [hqchen@gzu.edu.cn](mailto:hqchen@gzu.edu.cn) (H. Chen), [james.marrow@materials.ox.ac.uk](mailto:james.marrow@materials.ox.ac.uk) (T.J. Marrow).

good fire-resistance, and is a promising environment-friendly material [11,12]. MOC has good composite properties when combined with the plant fibres, and compared with silicate cement, the lower alkalinity of MOC is less corrosive to plant fibres [6,13]. Therefore, combining MOC with straw, sawdust and other plant fibres can give a construction material with low density and low production cost [14]. Wang et al. [2] reported a straw/magnesia light-weight composite which is an excellent construction material, and it exhibits better insulation and fire resistance than traditional construction materials. Zhou et al. [15] incorporated sawdust into MOC and obtained a low-cost, environmentally friendly and mass-produced lightweight material. Besides, the plant fibres can improve the mechanical properties of the MOC, for instance, Chen et al. [7] reported that the addition of both corn straw and sawdust increased the flexural strength of MOC.

According to the above, there are many environmental and health problems caused by straw and sawdust need to be solved, such as haze, fire hazard, and respiratory problems. Mixing straw and sawdust into cement to make building materials is a method that can solve the problems and generate economic benefits. At the same time, MOC has excellent properties and is friendly to plant fibres. Therefore, this paper is concerned with a new construction material that can realize the recycling of straw and sawdust by combining them with MOC. Since the appearance of the material is quite like wood, it is named 'magnesium-based wood-like material' (MWM). MWM can use a wide range of raw material sources. It has good thermal insulation, fire prevention and durability, and overcomes the shortcomings of natural wood materials. Using MWM as a substitute for commercial wood for building materials is conducive to the protection, preservation and development of wood structure buildings, and MWM has the potential for high significance in environmental protection and promoting carbon neutrality.

At present, there have been some research on MWM. Through SEM, Zhang et al. [16] concluded that the microstructure of MWM is flocculated, and the chemical crystals cannot completely fill the pores formed by fibre bridging, which affects the compressive performance of the material, and it is an objective phenomenon that is difficult to eliminate. He et al. [17] concluded that increasing the pressing pressure can effectively reduce the porosity, redistribute the pore size and refine the pore structure, thus significantly improve the compressive strength of MWM. Therefore, in present study, the external pressure during moulding was set to 3.3 MPa which is recommended by He et al. [17]. Besides, poor water resistance limited the application of MWM in engineering [6], He et al. [17] thought that improving the pressing pressure of MWM has no noticeable effect on its water resistance. For solving this problem, Yang et al. [6] studied the modification mechanism of the modifier on the properties of MWM, and concluded tartaric acid can improve the water resistance. Therefore, analytically pure tartaric acid is added to the material in present study. In terms of mechanical properties, Yang et al. [18] established constitutive model of the compressive stress-strain behavior of MWM, and the uniaxial compressive damage process of MWM was analysed based on acoustic emission results. Besides, Liu et al. [19] and Zhang et al. [16] both conducted preliminary studies on the compressive, tensile, and shear properties of MWM.

The above studies have made great contributions to the development of MWM. About the mechanical properties and failure mechanism of MWM, there is still a lack of comprehensive and intensive research, and there has been limited research on the failure process and the mechanisms of crack evolution in MWM. However, understanding of the initiation and propagation of cracks is an important aspect in fracture mechanics [20], and the failure mechanism under various loading conditions is important for the design and construction of structures [21]. Therefore, in present study, the mechanical properties and splitting tensile characteristics as well as the crack propagation rules of MWM are investigated. Meanwhile, reliable test method is critical to the analysis and design of the structural members made of the MWM. The Brazilian splitting test is an indirect method to estimate the tensile strength that has advantages of simple preparation of specimens, low cost and ease of operation [22,23]. Cylindrical or disc specimens are usually used in the Brazilian splitting test. However, for MWM, cubic specimens are more convenient to prepare in the laboratory, and cubic splitting tests can be performed as an alternative to Brazilian splitting test [24,25], so the splitting tensile test is carried out on cubes. As it is difficult to observe crack growth directly in this material, Digital Image Correlation (DIC) was used to study deformation and damage. DIC has advantages of simple setup and low cost, so it has been widely used in the testing of mechanical properties of civil engineering materials. DIC provides high-precision full-field displacements and its effectiveness in quantifying crack evolution has been confirmed in many studies [26–29].

To sum up, MWM is a significant and novel building material, the mechanical properties of MWM, such as the elastic Young modulus, Poisson's ratio and axial compressive strength were investigated in present study. Besides, splitting tensile tests were performed on cubic specimens and the DIC technique was used to measure the deformations. Firstly, the displacement and strain distributions on the specimen surface were analysed and the splitting tensile strength of the MWM was determined. Secondly, a new and accurate method for identifying crack modes has been proposed. The method is based on the local strain growth trend, and it is novel, robust and easy to operate. This method has never been used before. In present study, the method has been used in cubic splitting tensile tests to verify that the primary cracks were caused by tensile failure, and using the method, the main failure modes of secondary cracks were determined. Finally, a method for estimating the elastic Young modulus simultaneously with the splitting tensile strength of the MWM was proposed and calculation equations were modified based on the Cartesian coordinate system, which is suitable for cubic specimen. The proposed method is a supplement for the original method based on the polar coordinate system for disc specimen, which has the potential to estimate the material properties of other materials.

## 2. Materials and experimental tests

### 2.1. Specimen preparation

The preparation of MWM was as follows: The molar ratio of  $\text{MgO}:\text{MgCl}_2:\text{H}_2\text{O}$  was 11:1:19. Magnesium oxide powder was added to magnesium chloride solution with a waviness of  $23^\circ\text{Be}$  to produce a MOC net slurry that was stirred well using a mixer [6,17].

**Table 1**  
Properties of straw and sawdust.

Element	Moisture contents	Density / [g/cm <sup>3</sup> ]	Mud content	Particle size / [mm]
Straw	10.5%	0.24	< 1%	< 8
Sawdust	13.2%	0.30	< 1%	< 8

**Table 2**  
Chemical composition of light-burned MgO powder.

Oxide	MgO	Al <sub>2</sub> O <sub>3</sub>	SiO <sub>2</sub>	P <sub>2</sub> O <sub>5</sub>	SO <sub>3</sub>	K <sub>2</sub> O	CaO	Fe <sub>2</sub> O <sub>3</sub>	Others
Mass Fraction	91.093%	0.583%	5.766%	0.072%	0.072%	0.026%	1.997%	0.286%	0.105%



(a) Cubic specimens (100 × 100 × 100 mm<sup>3</sup>)



(b) Prism specimens (100 × 100 × 300 mm<sup>3</sup>)

**Fig. 1.** Appearance of MWM.

Straw/sawdust mixture, additive A and analytically pure tartaric acid were added to the MOC net slurry, with a mass ratio of 20%, 0.25%, and 0.25%, then stirred for 3 min to disperse. The mixture was poured into a mould (1500 × 1000 × 1000 mm<sup>3</sup>) and an external pressure of 3.3 MPa was applied for 24 h. The material was then demoulded and air cured for 28d at a temperature of 20 ± 3 °C and relative humidity of 70 ± 5%.

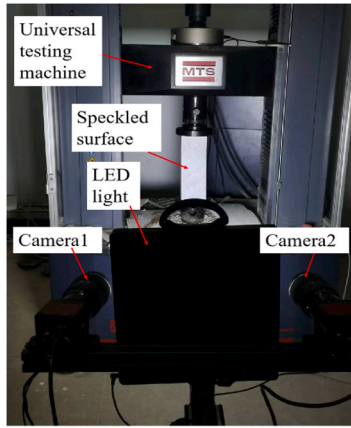
The moisture contents of straw and sawdust were 10.5% and 13.2% by mass, and the densities were 0.24 g/cm<sup>3</sup> and 0.30 g/cm<sup>3</sup>. Both of them had a mud content of less than 1%. The straw/sawdust mixture was crushed in a pulveriser and then sieved to a particle size of less than 8 mm. Straw and sawdust, without mould, decay, and other impurities, were provided by Guiyang Huaxi Yuanhai Wood Factory. And there were no stones, silt, and other contaminants to ensure the final quality of the material. The specific properties are shown in Table 1. Light-burned magnesium oxide was produced in Liaoning Province, China. Its purity was 91.09%, and the active content was 59.98%, and the chemical composition is shown in Table 2. Industrial magnesium chloride (MgCl<sub>2</sub>·6H<sub>2</sub>O) was produced in Qinghai Province, China, with 46% purity. Additive A was composed of 1:1 soluble sulphate and soluble phosphate at a concentration of 5%. Additive A was used to improve the water-resistance of MWM, and analytically pure tartaric acid was used to slow down the cement's hydration and reduce the hydration heat. The final density of the MWM was 1135.52 kg/m<sup>3</sup>.

The appearance of the MWM is shown in Fig. 1. A total of fourteen prism specimens (100 × 100 × 300 mm<sup>3</sup>) were prepared for the tests of basic mechanical properties; five specimens (EV1 to EV5) were used to determine the elastic Young modulus and Poisson's ratio and nine specimens (AC1 to AC9) were used for axial compression tests. A further seven cubic specimens (100 × 100 × 100 mm<sup>3</sup>) were prepared for the splitting tensile tests (ST1 to ST7). All tests were performed according to the National Standard for test methods of concrete physical and mechanical properties (GB/T 50081–2019) [30].

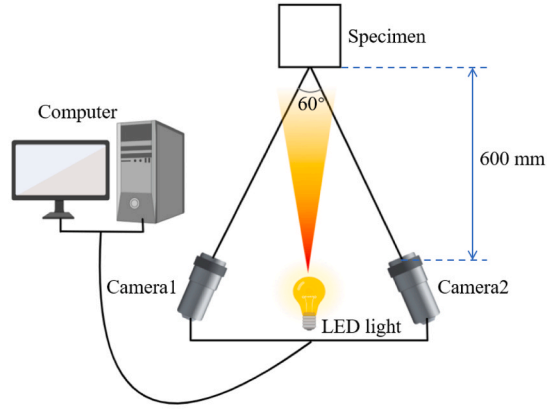
## 2.2. Experimental tests

The test setup (Fig. 2) consisted of a loading device (MTS microcomputer-controlled electronic universal testing machine) and a DIC system (light source, 2 cameras, a computer, and an image transmission device). Each camera was a Prosilica GE4900 with 4872 × 3248 pixels. An LED light was installed between the two cameras to maintain uniform illumination and reduce the effect of ambient light on the image quality.

The surface of the specimen was prepared for DIC by cleaning then coating with a uniform white spray paint followed by spray with black paint to produce a random speckle. DIC works by finding the maximum correlation between sub-windows of digital images of the

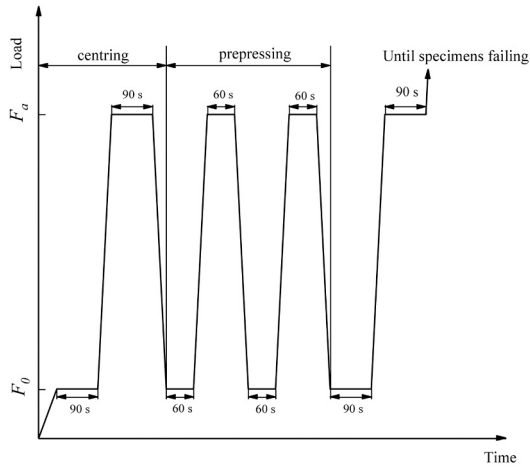
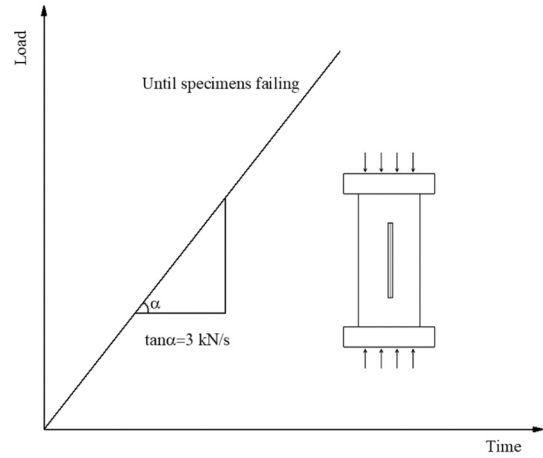


(a) Test setup (photograph)



(b) Schematic view of test setup

Fig. 2. Test setup.

(a) Test for  $E$  and  $\nu$ 

(b) Test for compressive strength

Fig. 3. Schematic loading modes for the different tests.

specimen in its undeformed and deformed state to provide the displacement field matrix [26,27]. The software VIC-3D was used to obtain the 2D displacement field of the observed surface. The precision was estimated to be about  $0.5 \mu\text{m}$  [31–33], which meets the requirements of this study.

#### 2.2.1. Basic mechanical properties tests

The loading applied to obtain the elastic Young modulus ( $E$ ) and Poisson's ratio ( $\nu$ ) is shown in Fig. 3a. The loading rate was  $3 \text{ kN/s}$ , and the camera sampling rate was  $1 \text{ fps}$ . To centre and prestress the specimen, the loading was varied over several cycles between the reference compressive stress ( $F_0$ ) of  $5 \text{ kN}$  and the maximum compressive stress ( $F_a$ ) of  $33 \text{ kN}$ . To obtain  $E$  and  $\nu$ , different virtual strain gauges were defined (Fig. 4a). A vertical gauge (VS1) with  $150 \text{ mm}$  length was defined for  $E$ . For  $\nu$ , vertical and transversal gauges (VS2 and VS3) near the center of the specimen were defined with lengths of  $50 \text{ mm}$ . The specimens were then loaded to failure, and the failure loads were not used to calculate the compressive strength due to possible effects of the prior load cycles.

The values of  $E$  and  $\nu$  were calculated according to Eq. 1 and Eq. 2 for the last prestressing cycle between the reference and maximum stress levels.

$$E = \frac{F_a - F_0}{A} \times \frac{L}{\Delta n} \quad (1)$$



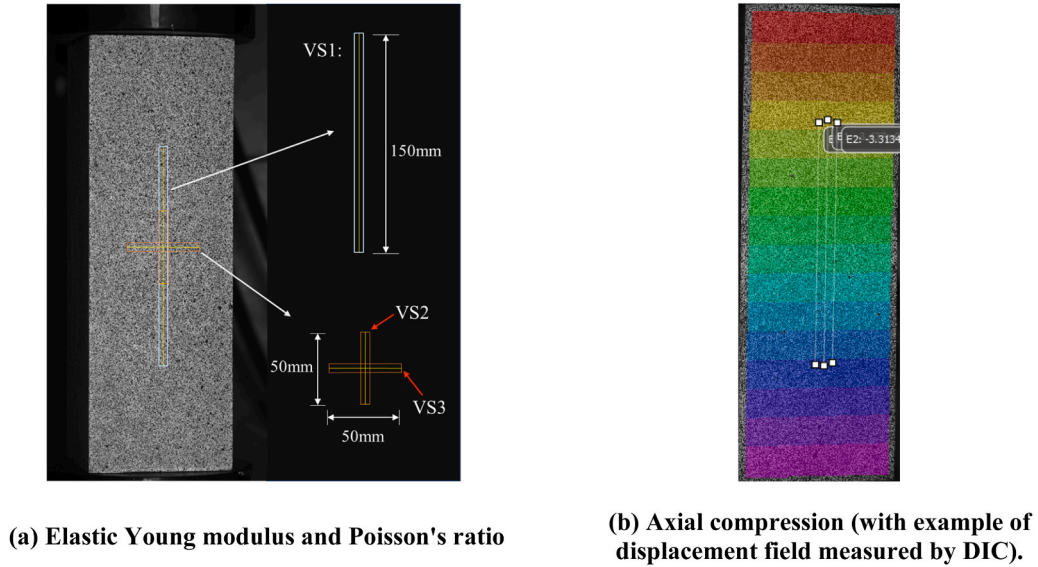


Fig. 4. Monitoring positions of virtual strain gauges.

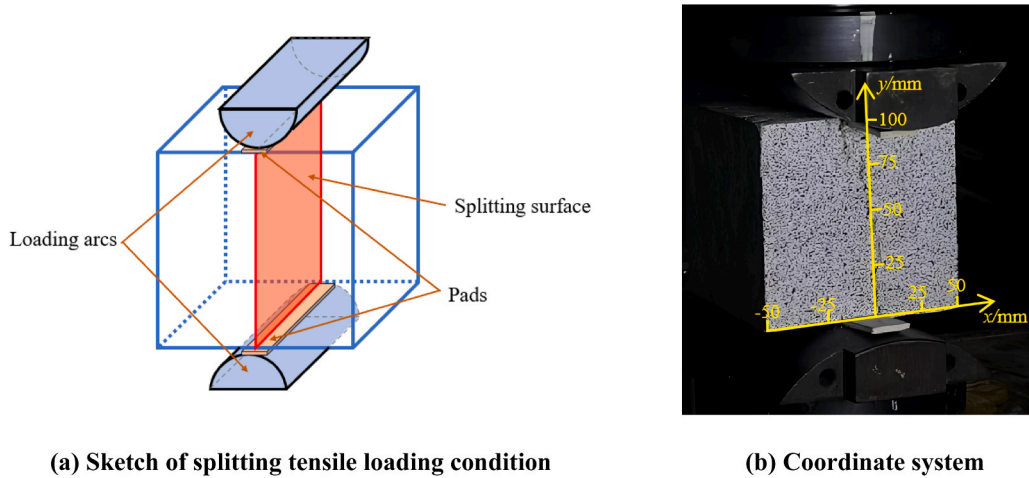


Fig. 5. Splitting tensile loading condition and coordinate system.

$$\nu = \frac{\epsilon_{ha} - \epsilon_{h0}}{\epsilon_{va} - \epsilon_{v0}} \quad (2)$$

Where  $A$  is the area of the pressure-bearing surface (i.e. the cross section of the specimen);  $L$  is the length of the virtual strain gauge;  $\Delta l$  is the change of the gauge length when it is loaded from  $F_0$  to  $F_a$ .  $\epsilon_{ha}$  is the average transverse strain at  $F_a$ .  $\epsilon_{h0}$  is the average transverse strain at  $F_0$ .  $\epsilon_{va}$  is the average vertical strain at  $F_a$ .  $\epsilon_{v0}$  is the average vertical strain at  $F_0$ .

For the compressive strength tests, the specimen was loaded to failure directly at 3 kN/s (Fig. 3b). The monitoring positions of vertical strain are shown in Fig. 4b, and the axial compressive strength was calculated according to Eq. 3 [30].

$$f = 0.95 \frac{F}{A} \quad (3)$$

Where  $f$  is the axial compressive strength;  $F$  is the failure load;  $A$  is the area of the pressure-bearing surface; 0.95 is the size conversion factor for specimens of  $100 \times 100 \times 300 \text{ mm}^3$  size according to GB/T 50081–2019 Standard for test methods of concrete [30].

### 2.2.2. Splitting tensile tests

The loading condition for the splitting tensile test is shown in Fig. 5. Loading arcs and pads were placed on the upper and lower surfaces of the specimens, aligned with the centre line [30,34]. The loading arc was a convex steel block with 75 mm radius (Fig. 5a).

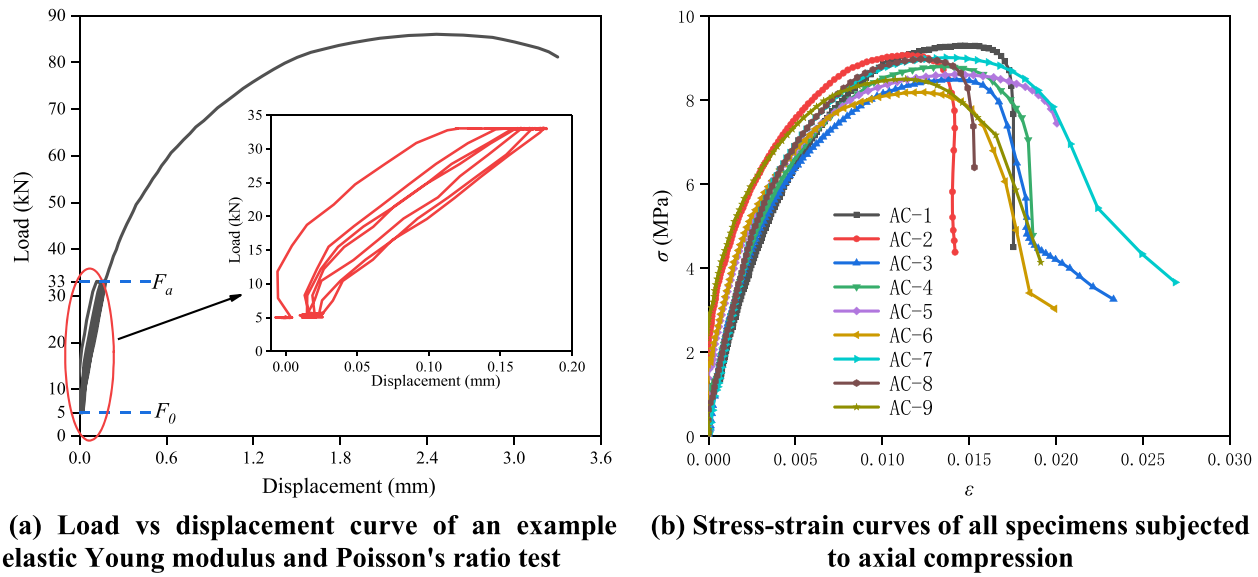


Fig. 6. Basic mechanical property tests.

**Table 3**  
Elastic Young modulus and Poisson's ratio.

Specimen	Failure load / [kN]	$E$ / [GPa]	Average ( $E$ ) / [GPa]	Standard deviation ( $E$ ) / [GPa]	$\nu$	Average ( $\nu$ )	Standard deviation ( $\nu$ )
EV1	88.505	1.846	2.210	0.279	0.172	0.208	0.033
EV2	102.730	2.605			0.174		
EV3	99.161	2.317			0.232		
EV4	95.928	2.342			0.258		
EV5	90.844	1.943			0.201		

**Table 4**  
Axial compressive strength.

Specimen	Cross section in compression size / [mm <sup>2</sup> ]	Failure load / [kN]	Axial compression strength / [MPa]	Average strength/ [MPa]	Standard deviation/ [MPa]
AC1	101.28 × 103.50	102.476	9.29	8.76	0.33
AC2	101.75 × 101.04	98.084	9.06		
AC3	101.46 × 100.40	91.035	8.49		
AC4	101.46 × 103.06	96.748	8.79		
AC5	101.01 × 101.67	92.982	8.60		
AC6	100.85 × 102.03	88.575	8.18		
AC7	101.54 × 101.44	97.617	9.00		
AC8	104.15 × 99.47	97.761	8.96		
AC9	105.06 × 98.55	92.564	8.49		

The pad, which was placed between the arc and specimen, was ordinary plywood with a width of 20 mm and a thickness of 2 mm. The force from the testing machine was loaded to the pad through the loading arc, and then to the MWM specimen. This made a uniform force with a width of 20 mm and the length of 100 mm. The width ratio, i.e. the ratio of the contact width between the pad and the specimen to the width of the specimen, was 20%. The loading was force controlled with a rate of 200 N/s and the camera sampling rate was 2 fps. The coordinate system is shown in Fig. 5b, where the intersection line between the splitting surface and the observed speckled surface is the Y-axis and the bottom edge is the X-axis.

### 3. Results and discussion

#### 3.1. Test results

##### 3.1.1. Basic mechanical properties

An example load vs displacement curve in a test to obtain the elastic Young modulus and Poisson's ratio is shown in Fig. 6a. Stress vs strain curves of axial compressive strength tests are shown in Fig. 6b. The mean elastic Young modulus was 2.210 GPa, with a standard deviation of 0.279 GPa. Poisson's ratio was 0.208, with a standard deviation of 0.033. The mean axial compressive strength was 8.76 MPa, with a standard deviation of 0.33 MPa. The individual specimen data for the elastic Young modulus and Poisson's ratio are shown in Table 3, and the axial compressive strengths are reported in Table 4.

The load-displacement curves of different loading cycles in the tests to obtain the elastic Young modulus and Poisson's ratio are almost coincident, except for the first cycle (Fig. 6a). The first loading involves surface compaction at the anvil contacts, and there is then no change in the residual displacement in subsequent cycles. The hysteresis curves between  $F_0$  to  $F_d$  are almost parallel in each cycle. This means that the specimen is essentially elastic over this range, and the evaluation of  $E$  and  $\nu$  in the last prestressing cycle between the reference and maximum stress levels is appropriate. The geometric characteristics of stress-strain curves to failure are similar for all specimens (Fig. 6b). The rate of change is large at first, and then gradually decreases. After the peak of the compressive strength, the stress decreased sharply.

##### 3.1.2. Splitting tensile tests

In the test standard [30], the splitting tensile strength of the cubic specimen is obtained using the same theoretical formula as for the Brazilian splitting test of a disk:

$$f_{ts} = \frac{2F_t}{\pi A_t} \quad (4)$$

Where  $f_{ts}$  is the splitting tensile strength;  $F_t$  is the failure load of the specimen;  $A_t$  is the area of the splitting surface.

Eq. 4 is derived from the analytical elastic solution given by Muskhelishvili [35], and Qu obtained the same expression using the Griffith fracture criterion [36,37]. Both solutions are for a disk splitting test under a concentrated force. Based on the theory of complex variable functions, Cheng obtained an analytical elastic solution for the stress distribution in the cubic specimen under both concentrated (Fig. 7a) and uniform forces (Fig. 7b) where the uniform stress is distributed along the center part with a width ratio within 5%~30% [38]. Cheng's predicted stress distributions, normal to the splitting surface, are shown in Fig. 7c. The distance from

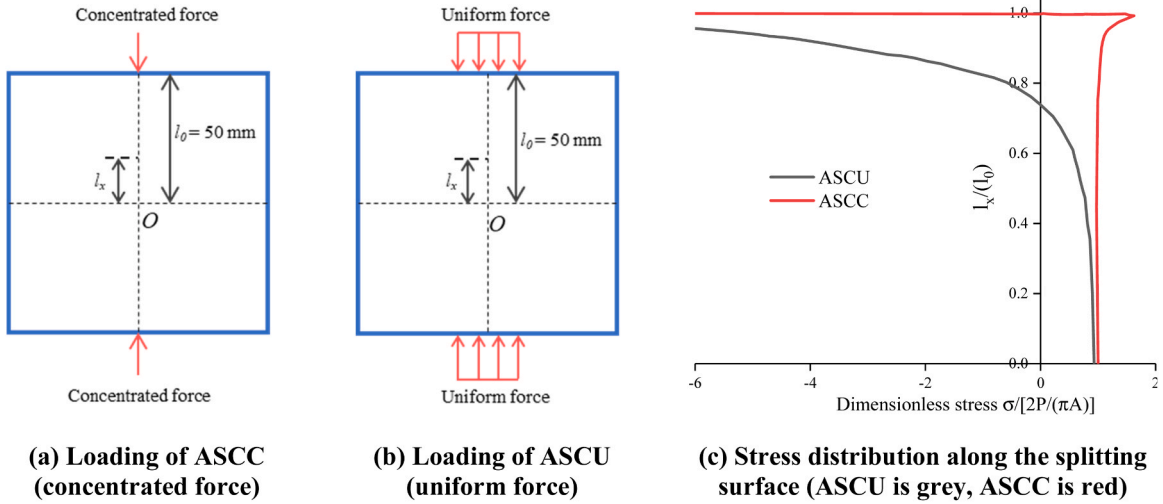


Fig. 7. Loading conditions and stress distribution.

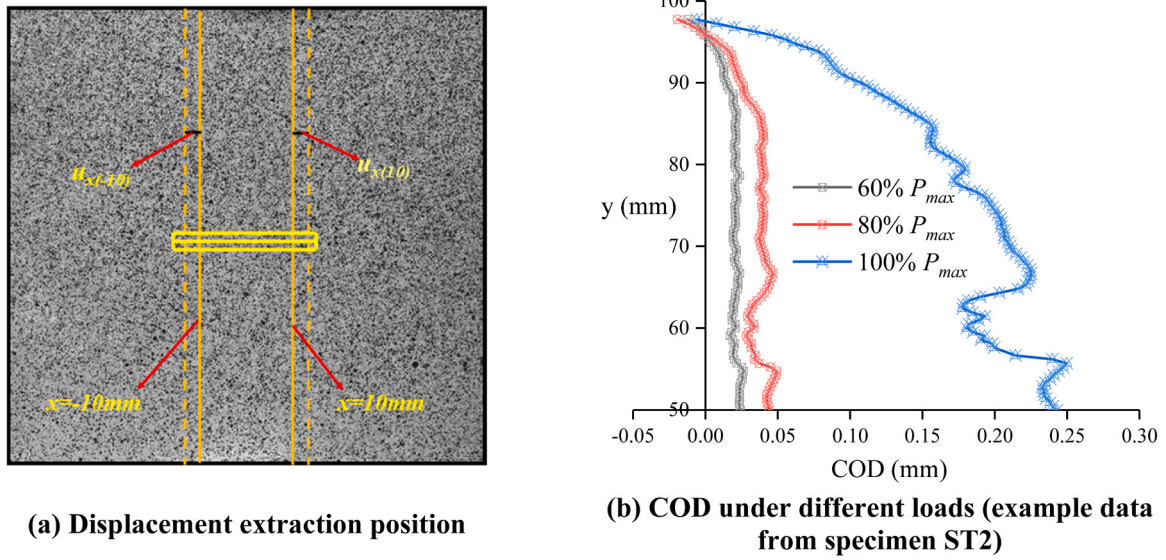


Fig. 8. COD of the splitting surface.

the centre point is  $l_x$ ,  $l_0 = 50\text{mm}$  and the abscissa is the dimensionless stress (i.e.  $\sigma/[2P/(\pi A)]$ ). For convenience, the present study names the analytical solution of cubic splitting under a concentrated force as ASCC, and the analytical solution of cubic splitting under a uniform force as ASCU. For ASCU, the predicted tensile stress gradually decreases from the centre point to the loading end, and then becomes compressive. For ASCC, the predicted tensile stress decreases slightly (by 4.08%) then increases from the centre point to the loading end, it drops sharply after reaching the maximum, and then becomes infinitely compressive in this model.

The ASCU stress distribution appears well suited to obtain the splitting tensile strength as there is a significant volume at the centre of the specimen with high tensile stress, but it is necessary to verify that it provides a satisfactory description of the MWM cubic splitting test. It is difficult to directly measure the stress in real-time (such as by diffraction [39]), so the present study has analysed the centreline opening displacement (COD) of the specimen surface. Before crack nucleation, the COD should depend on the elastic strains due to the tensile stress distribution. Once a crack has initiated, the centreline opening displacement is noted as crack opening displacement: Alam et al. used DIC measurement of the displacements on either side of a crack to obtain crack opening displacement [40], and Scotson et al. used full field displacements both to quantify the crack opening and to evaluate the fracture toughness [41]. In this study, the COD,  $u_{xi}$ , was extracted from the DIC displacement field as follows.

$$u_{xi} = u_{x(10)i} - u_{x(-10)i} \quad i = 1, 2, 3, \dots, 299, 300 \quad (5)$$

**Table 5**  
Splitting tensile strength.

Specimen	$A_t$ / [mm <sup>2</sup> ]	$P_{max}$ / [kN]	Proportional limit	$\sigma_{lim.}$ / [MPa]	$f_{ts}$ / [MPa]	Average strength/ [MPa]	Standard deviation/ [MPa]
ST1	101.23 × 98.48	33.372	40.66% $P_{max}$	0.81	1.99	1.79	0.12
ST2	103.49 × 102.14	32.944	36.95% $P_{max}$	0.68	1.85		
ST3	104.52 × 102.12	34.169	41.51% $P_{max}$	0.79	1.90		
ST4	105.38 × 102.73	31.273	35.94% $P_{max}$	0.62	1.72		
ST5	103.24 × 101.46	29.312	32.69% $P_{max}$	0.54	1.66		
ST6	105.08 × 101.92	32.481	30.64% $P_{max}$	0.55	1.80		
ST7	103.42 × 100.37	28.606	35.32% $P_{max}$	0.58	1.64		

Where;  $u_{x(-10)i}$  is the displacement of each point on the line  $x = -10$  mm in the X-direction;  $u_{x(10)i}$  is the displacement of each point on the line  $x = 10$  mm in the X-direction (Fig. 8a). There are 300 data points on each line.

As shown in Fig. 8b, the COD curve up to maximum load ( $P_{max}$ ) conformed to that expected for a cubic specimen under uniform distributed force (ASCU). The COD was largest at the centre of the specimen; it gradually decreased to the loading ends and then became negative. The maximum COD increased significantly as failure was approached (i.e. between 80% and 100%  $P_{max}$ ).

Following Cheng's solution for ASCU [38], the stress correction coefficient is 0.932 for width ratio of 20%, so the splitting tensile strength was obtained by Eq. 6:

$$f_{ts} = \frac{1.864F_t}{\pi A_t} \quad (6)$$

Where  $f_{ts}$  is the splitting tensile strength;  $F_t$  is the failure load;  $A_t$  is the area of the splitting surface. The mean splitting tensile strength was 1.79 MPa, and the standard deviation was 0.12 MPa (Table 5).

To investigate the stress-strain response of the cubic specimens in the splitting test, the strains at the centre of the specimens in the X-direction was obtained from the DIC displacement, with a horizontal virtual strain gauge length of 30 mm at the height of  $Y = 50$  mm, cantered along the splitting line. The strains are obtained using the net displacement change across the 30 mm gauge. The stress-strain relationships were shown Fig. 9a, and an example of the variations of strain and strain rate with time at this central location is shown in Fig. 9b. This shows the splitting tensile failure process can be divided into three stages.

In the first stage, the stress-strain curve is linear, and presumed to be elastic. The extent of the elastic stage can be determined using the strain rate. As shown for the example in Fig. 9b, the strain rate is almost constant for approximately 60 s at which the corresponding load is 36.95%  $P_{max}$ , which is judged to be the proportional limit where the tensile stress  $\sigma_{lim.} = 0.68$  MPa. The proportional limit of all specimens ranged from 30.6%  $P_{max}$  to 41.5%  $P_{max}$ , so the proportional limit stress,  $\sigma_{lim.}$  was between 0.54 and 0.81 MPa (Table 5). Below the proportional limit, a strain concentration may be observed at the specimen centre (Fig. 10a) that causes the COD variation (Fig. 8b). The second stage beyond the proportional limit is 'damage accumulation'. Here, the deformation is nonlinear, although no macroscopic cracking was observed. The strain concentration at the specimen centre is more significant in this stage (Fig. 10b), with the corresponding increase in COD (Fig. 8b). In the third 'cracking' stage above 80%  $P_{max}$ , macroscopic cracks appear and the strain concentration becomes more significant (Fig. 10c and Fig. 10d).

Plain concrete is the most versatile construction material [42], its characteristics have great reference value for other new materials. In this paper, the characteristics of MWM in splitting are compared with those of concrete. The stress-strain curves show there is a capacity to sustain stress after the peak load, whereas in plain concrete splitting test the stress falls rapidly after reaching the peak [43,44]. In these tests of MWM, the COD at  $P_{max}$  is about 250  $\mu$ m (Fig. 8b), whereas in similar tests of concrete without plant fibres it is about 100  $\mu$ m [45]. This further indicates that the toughness of MWM is improved relative to plain concrete.

The failure process can be examined in more detail (Fig. 11). As the load approached  $P_{max}$ , a primary crack appeared in the geometric centre of the specimen (Fig. 11b). The central location of the crack coincided with the strain concentration observed at lower loads (Fig. 11a) and also the predicted location of maximum tensile stress. After the peak load, the primary cracks extended rapidly (Fig. 11c and Fig. 11d) and then strain concentrations and secondary cracks were observed to develop near the pads (Fig. 11e and Fig. 11f).

### 3.2. Identification method for crack mode

The cracks (either tensile or shear) are responsible for low strengths and weak mechanical resistances of materials [46]. It is generally considered that the formation of the primary crack in the centre of the specimen is due to the tensile stress along the central vertical splitting surface, while the formation of the secondary crack near the loading pads is more complicated [47,48]. Different crack modes may lead to differences in the macroscopic behavior of the material, such as the rate of crack extension or dimensional



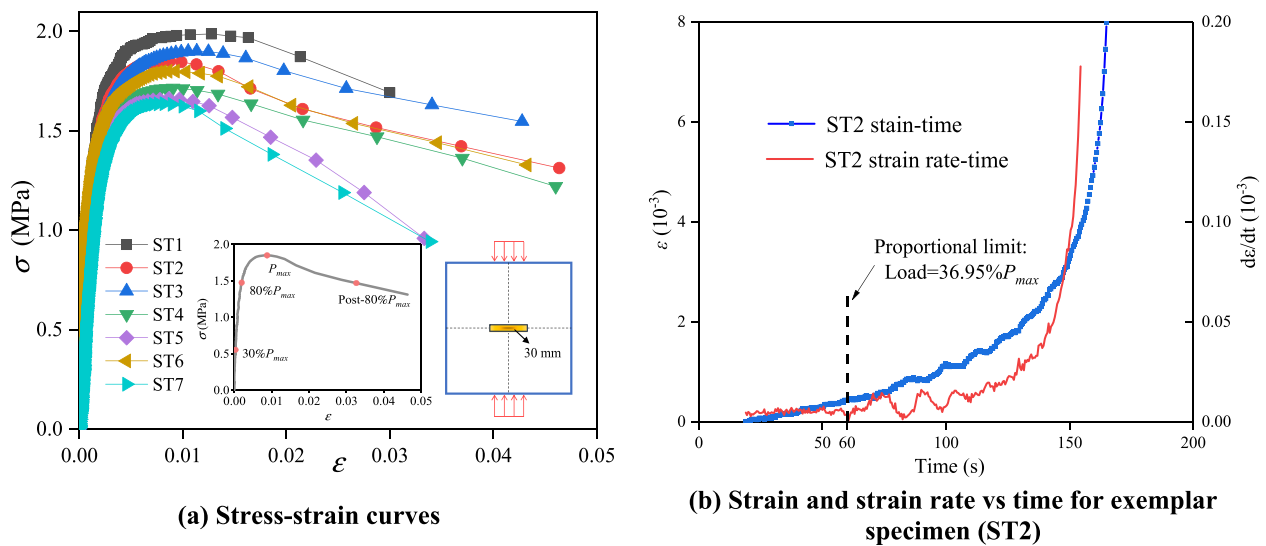


Fig. 9. Stress-strain response in splitting tensile test.

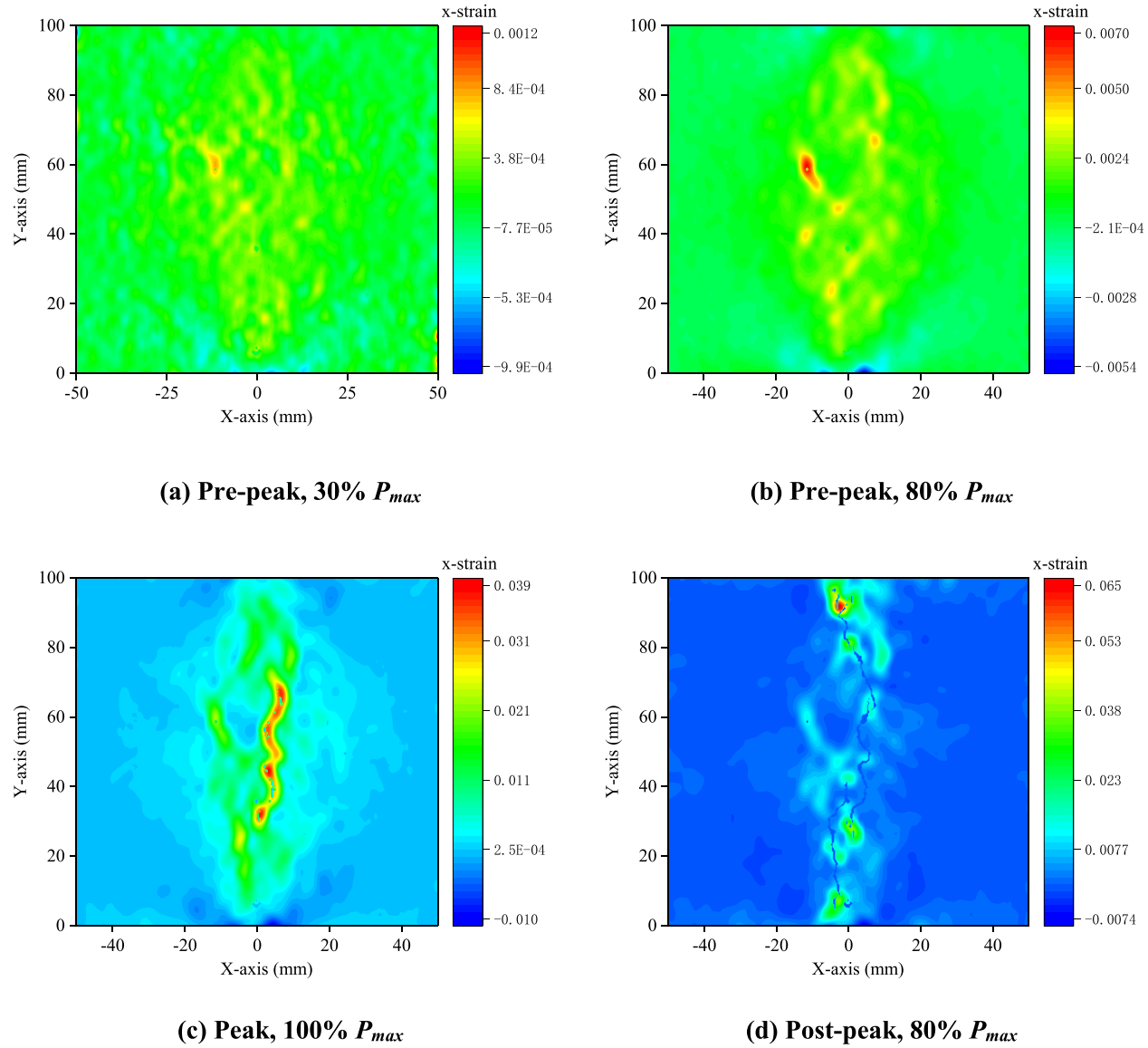


Fig. 10. Strain contours in each stage for exemplar specimen (ST2).

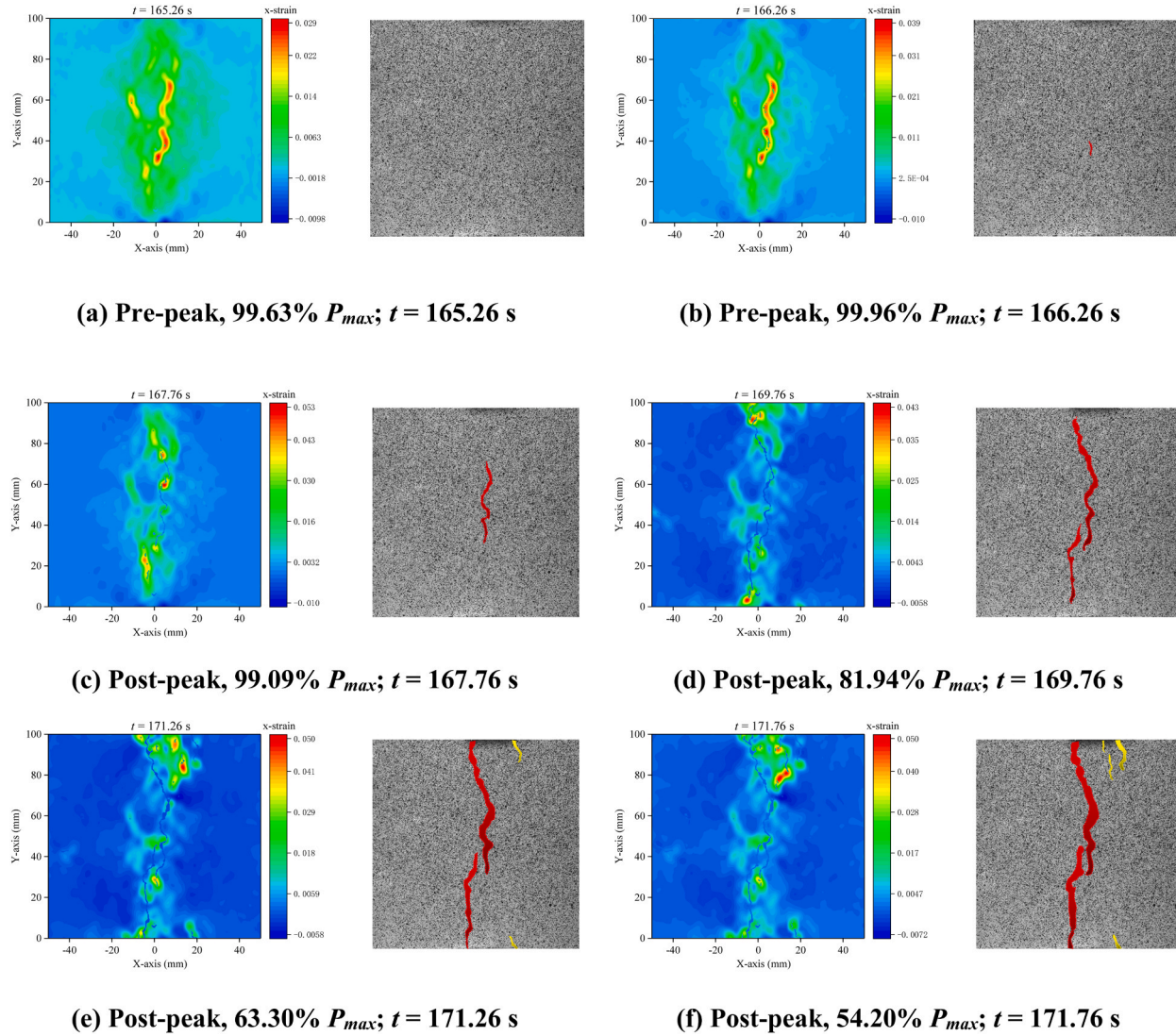


Fig. 11. Strain fields and cracks ('primary' red and 'secondary' yellow) during failure of exemplar specimen (ST2).

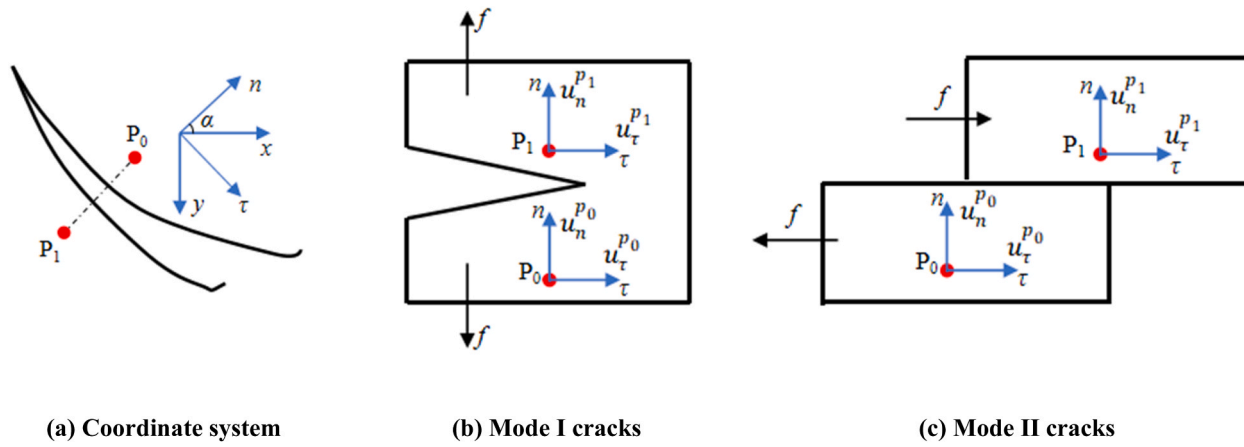


Fig. 12. Displacement Judgement Method (DJM) for crack modes.

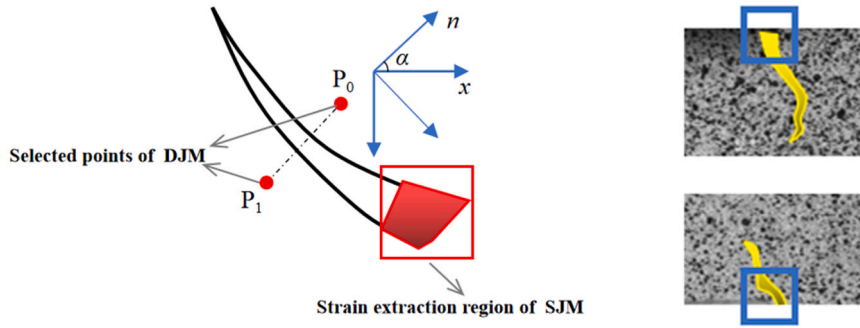


Fig. 13. Strain extraction region of the Strain Judgement Method (SJM) for crack modes.

change in the fracture process zone [49]. Therefore, study of the mechanisms of the secondary cracks is important for understanding the failure process of MWM. The deformations at the loading ends were complex, so it is necessary to identify the crack modes through analysis of the experimental data. According to different loading conditions, there are generally three basic modes of cracks, which are mode I (opening mode), mode II (shearing Mode) and mode III (tearing Mode) [50].

Conventionally, the modes of cracking in brittle materials are judged subjectively by fractographic appearance with a simple classification as mode I tensile cracks if the crack surface is clean or accompanied by a plume structure, and mode II shear cracks if the surface is rough or covered with pulverized powder [51–53]. This method is widely used, for example, Sarfarazi et al. used the fractographic appearance to determine the fracture mode of END plexiglass [54]. The mode of cracking can also be characterized by analysis of the relative displacement across a crack [55], or analysis of the crack displacement field to evaluate the J-integral and then extract the mixed mode stress intensity factors [56–58]. For practical tests, it is useful to have robust methods that are simple to apply. Liu et al. [29] proposed a method for the identification of the crack mode using DIC observations of the specimen surface displacement field. Based on that work, a new identification method is proposed in the present study. This has been applied to the secondary cracks in the splitting test of the MWM cube and compared with Liu's to demonstrate its effectiveness.

Liu et al. [29] determined the crack modes by using the relative displacement between two points, at  $P_0$  and  $P_1$ , on a line orthogonal to the crack. This was done by first ascertaining the position and the angle of the crack in the DIC coordinate system ( $xy$ ). A conversion was then done into the  $n\tau$  coordinate system, with the  $n$ -axis normal to the line  $P_0P_1$ . Finally,  $\Delta u_n$  (the normal relative displacements) and  $\Delta u_\tau$  (tangential relative displacements) were calculated. If  $\Delta u_n$  is larger than 0 while  $\Delta u_\tau$  is small, it is classified as a mode I crack. If  $\Delta u_n$  is less than or equal to 0 and  $\Delta u_\tau$  has magnitude larger than 0, it is classified as a mode II crack. The method is shown schematically in Fig. 12. The parameters  $\Delta u_n$  and  $\Delta u_\tau$  are defined in Eq. 7 and Eq. 8. Since the crack mode is judged using relative displacements in the method of Liu et al., it is referred to in this paper as the Displacement Judgement Method (DJM). The advantage of DJM is that the locations of the selected data points are on either side of the crack where no damage occurs.

$$\Delta u_n = u_n^{P_1} - u_n^{P_0} \quad (7)$$

$$\Delta u_\tau = |u_\tau^{P_1} - u_\tau^{P_0}| \quad (8)$$

However, there are some drawbacks to DJM. The selection of the data points is arbitrary, and the line connecting the two selected points may not be perpendicular to the crack if its propagation path is not straight, which means an incorrect coordinate system will be established as the maximum  $\Delta u_n$  may not be orthogonal and the maximum  $\Delta u_\tau$  may not be parallel to the macroscopic crack. In order to overcome these problems, a novel Strain Judgement Method (SJM) for identifying crack modes based on the local strain trends was proposed. The SJM uses  $e_1$  (the principal tensile strain) and  $e_\tau$  (the maximum shear strain) in the cracked region as the main criteria. The strain extraction region is the crack initiation location, as shown in Fig. 13. In addition to the simplicity of operation, SJM does not require coordinate conversion and it directly considers the strain state at the crack to give a direct assessment of the crack modes.

Mode I crack propagation is considered to occur when the maximum tensile strain exceeds a critical threshold. In that condition,  $e_1$  is larger than 0 and  $e_\tau$  is approximately equal to 0 (satisfying Eq. 9). Alternatively, when the maximum shear strain exceeds a critical threshold, mode II crack propagation is considered to occur, such that  $e_\tau$  is larger than 0 and  $e_1$  is approximately equal to 0 (satisfying Eq. 10).

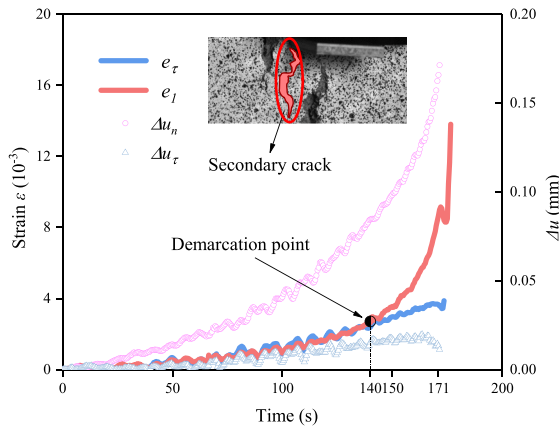
$$e_1 > 0 \cup e_\tau \approx 0 \quad (9)$$

$$e_1 \approx 0 \cup e_\tau > 0 \quad (10)$$

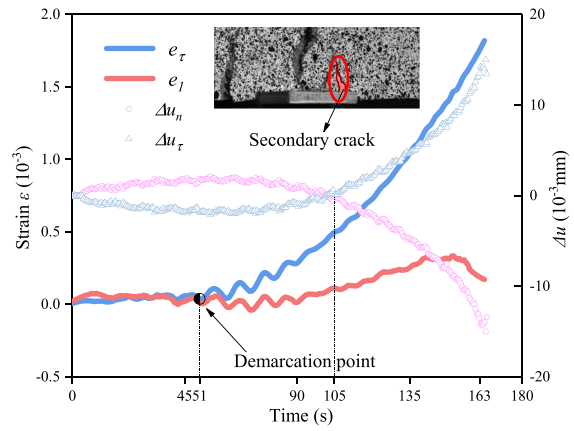
Where,  $e_1$  is the principal tensile strain;  $e_\tau$  is the maximum shear strain.

It is worth noting that it is difficult to predict the location of crack initiation during the loading process of physical test, thus the crack modes cannot be identified in real time. To identify crack modes, DIC technology was used to record the deformation of specimens' surface during the whole process. When the test was completed, the strain fields could be obtained by the post-processing software and the crack modes could be identified using the SJM.

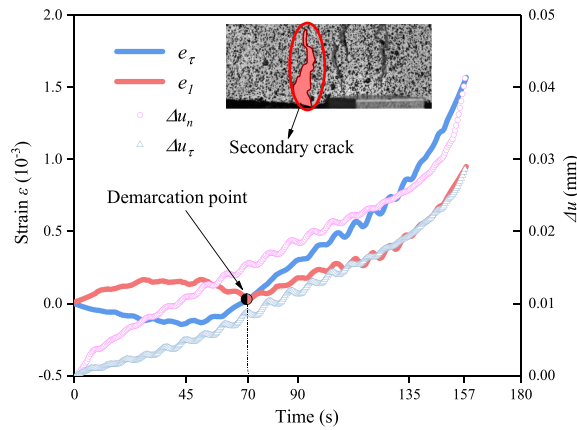




(a) A mode I Crack in ST3



(b) A mode II Crack in ST6



(c) A mixed mode I/II crack in ST4

Fig. 14. Examples of crack modes, evaluated by DJM and SJM.

### 3.3. Analysis of fracture modes in the present study

Example cracks (specimens ST3, ST4, and ST6) were assessed to demonstrate the judgement of crack modes using both SJM and DJM. Fig. 14a shows an example at the location of a Mode I secondary crack. Using the SJM analysis,  $e_1$  and  $e_r$  at this location both increased slowly from the beginning of loading. After about 140 s ('demarcation point'), the slope of the  $e_1$  curve increased steeply, while that of  $e_r$  remained stable. This is also apparent using the DJM analysis, where the growth of  $\Delta u_n$  accelerated with a value much larger than  $\Delta u_r$ , while  $\Delta u_r$  remained constant. Fig. 14b shows an example of a mode II secondary crack. Using the SJM analysis,  $e_1$  and  $e_r$  were stable at the beginning of loading, and then after about 62 s ('demarcation point'), the  $e_r$  curve increased steeply, while  $e_1$  remained stable. This is also shown by the DJM analysis in which both  $\Delta u_n$  and  $\Delta u_r$  were stable at the beginning of loading. After 105 s,  $\Delta u_n$  changed rapidly towards negative values (indicating that both sides of the crack were tending relatively inwards), while  $\Delta u_r$  increased rapidly due to shearing. Finally, Fig. 14c shows an example of a mixed mode I/II crack for which the SJM analysis shows essentially the same trends of  $e_1$  and  $e_r$ . For the DJM analysis crack, both  $\Delta u_n$  and  $\Delta u_r$  increased similarly due to opening and shearing.

These examples showed that the SJM provided accurate results which were equivalent to that using the DJM, but the SJM is simpler and more robust. A total of 18 secondary cracks were observed in all the tests, finding 3 mode I cracks, 8 mode II cracks and 7 mixed mode I/II cracks. The results show that the secondary cracks are mainly caused by shear failure and tensile-shear failure.

The crack modes of primary cracks were also examined using the SJM analysis, as illustrated in Fig. 15 for the example of specimen ST2. Analysis of all tests confirmed that the primary crack of each specimen was a mode I crack. This shows that the loading method in the present study is reliable for measurement of the tensile strength of MWM, as it causes splitting tensile failure of the specimens by mode I cracking.

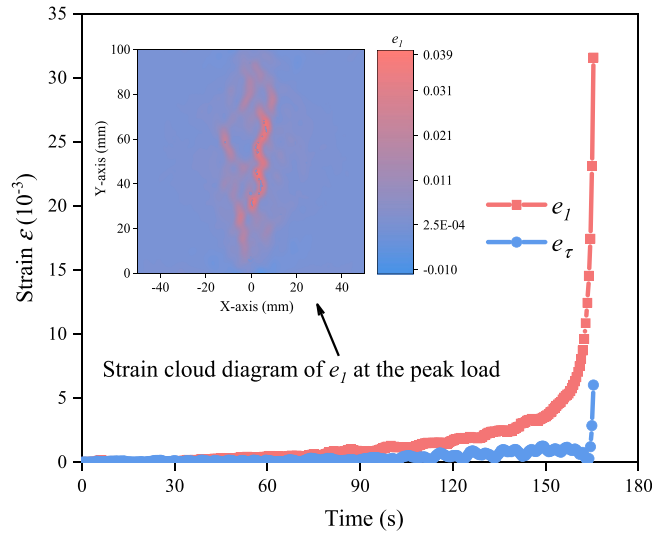


Fig. 15. Mode I in primary crack (specimen ST2), demonstrated by SJM.

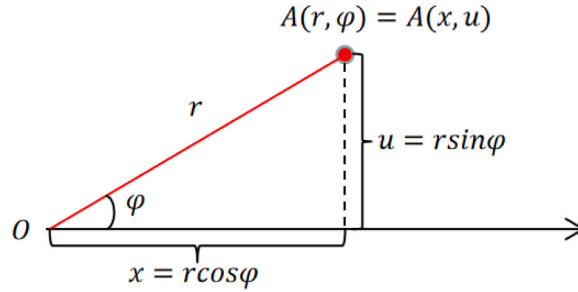


Fig. 16. Modification of Eq. (11) from polar to cartesian coordinates.

### 3.4. Estimation of the elastic Young modulus

The splitting test is performed to obtain the tensile strength of a material. However, the observation of the displacement field also offers the possibility to determine the elastic properties. Joyce et al. [59] used an inverse finite element analysis of the displacement field measured by ESPI, and concluded the elastic Young modulus and Poisson's ratio may be successfully derived from disc compression samples by mapping of the surface fields during loading. Jemioło et al. [60] also proposed that the elastic constants of brittle materials could be determined in Brazilian splitting tests, and based on that, Małyszko et al. [25] proposed a method to determine the elastic modulus and Poisson's ratio simultaneously, which was applied to autoclaved aerated concrete. In this study, we have developed the solutions of Jemioło and Małyszko as follows. In those works [25,60], the specimen were cylinders, and in the polar coordinate system  $(r, \varphi)$ , the displacements are:

$$u_x = \frac{P}{\pi L E} \left[ (1 - \nu) \left( \frac{r}{R} - 2 \arctg \frac{r}{R} \right) + (1 + \nu) \frac{2 R r}{R^2 + r^2} \right] \quad (11)$$

Where  $u_x$  represents the displacement in the X-direction of each point on the horizontal centre line;  $x$  is the corresponding horizontal coordinate;  $P$  is the load;  $L$  is the length of the specimen;  $R$  is the radius of the circular section;  $E$  is the elastic Young modulus, and  $\nu$  is the Poisson's ratio.

We have modified the above solution to obtain an implicit function for the displacements in the X-direction, so it could be applied to cube specimens for which the Cartesian coordinate system is more appropriate. The modified equation is as follows:

$$A(x, u) = A(r, \varphi) \quad (12)$$

$$\begin{cases} x = r \cos \varphi \\ u = r \sin \varphi \end{cases} \quad (13)$$

The modified equation is as follows:

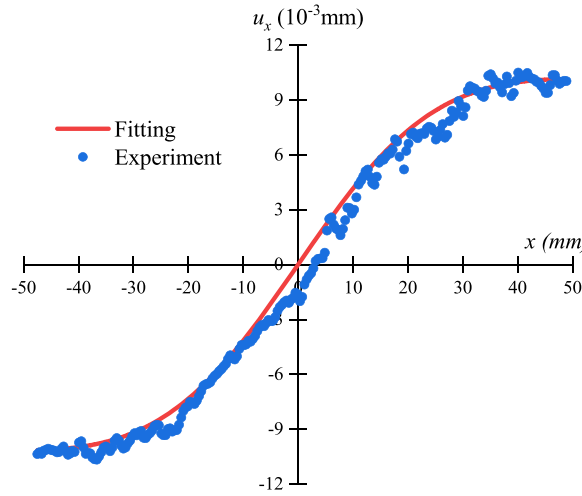


Fig. 17. Example of fitted curve for theoretical horizontal displacement with the DIC field (specimen ST3).

$$u = \frac{P}{\pi LE} \left[ (1 - \nu) \left( \frac{2\sqrt{x^2 + u^2}}{L} - 2\arctan \frac{2\sqrt{x^2 + u^2}}{L} \right) + (1 + \nu) \frac{L\sqrt{x^2 + u^2}}{\frac{L^2}{4} + x^2 + u^2} \right] \quad (14)$$

Where  $u$  represents the displacement in the  $X$ -direction of each point on the horizontal centre line ( $Y = 50$  mm);  $x$  is the corresponding horizontal coordinate;  $P$  is the load;  $L$  is the length of the sides of the cubic specimen;  $E$  is the elastic Young modulus, and  $\nu$  is the Poisson's ratio. Using this method, the splitting tensile strength and the elastic Young modulus of the cubic specimen can be obtained simultaneously through single test.

To ensure the accuracy of the method. The goodness of fit ( $R^2$ ) is used to judge the fitting results. Defining  $y = [u_1, \dots, u_n]$  as the observed value,  $u' = [u'_1, \dots, u'_n]$  as the fitted value, as well as  $\bar{u} = \frac{1}{n} \sum_{i=1}^n u_i$ .  $R^2$  is defined in Eq. 15.

$$R^2 = 1 - \text{RSS}/\text{TSS} \quad (15)$$

Where,  $\text{RSS} = \sum_i (y_i - y')^2$  is the residual sum of squares, and reflects the total variation of the estimated value of the dependent variable;  $\text{TSS} = \sum_i (y_i - \bar{y})^2$  is the total sum of squares, and reflects the total variation of observed values of dependent variable; In the best case, the fitting results match the theoretical values exactly,  $\text{RSS} = 0$  and  $R^2 = 1$ .

An analysis of variance (ANOVA) was conducted on the fitting results, and the results of  $F$ -test were used to test the significance of the whole model. According to the source of variance, the data were divided into two groups, regression and residual error.  $D_{f-\text{reg}}$  and  $D_{f-\text{res}}$  were the degrees of freedom of the two groups. The parameter  $F$  is defined in Eq. 16.

$$F = \text{MSR}/\text{MSE} \quad (16)$$

Where,  $\text{MSR} = \text{TSS}/D_{f-\text{reg}}$ ,  $\text{MSE} = \text{RSS}/D_{f-\text{res}}$ .

The  $P$ -value represents the overall error probability. (Both  $F$  and  $P$ -value were calculated in the software Origin, the larger the  $F$ , the smaller the  $P$ -value, the more significant the fit. Generally,  $P < 0.05$  is acceptable as a test for significance).

Besides, the Mean Percentage Error (MPE) was defined (Eq. 17) to show the difference between the mean value of the elastic Young modulus obtained by fitting to the splitting tensile test and the mean value obtained in the axial compression tests (Table 3).

$$\text{MPE} = \frac{100\%}{n} \sum_{i=1}^n \frac{E_i - E_{\text{exp}}}{E_{\text{exp}}} \quad (17)$$

Where,  $E_i$  is the result of the  $i$ th fit to the splitting tensile experiment;  $n$  is the total number of fits;  $E_{\text{exp}}$  is the mean value of the elastic Young modulus obtained by the axial compression experiments.

Two-parameter fitting between the theoretical equation and the displacement field measured by DIC in the linear region was used to find the elastic Young modulus and Poisson's ratio for all the splitting tensile tests. The Levenberg-Marquardt algorithm [61] was used for fitting, and Fig. 17 shows an example for specimen ST3. The results, obtained for each specimen using the displacement field at 30%  $P_{\text{max}}$  load are summarised in Table 6.

Each fit was successful and a suitable elastic Young modulus result was obtained. All the fits have large  $F$  values, while the  $P$ -values are much less than 0.05, and each goodness of fit is higher than 0.9. The results indicated that the model fit well and have strong

**Table 6**  
Fitting results.

Fit	Elastic constants		Goodness of fit		F-test	
	$E$ / [GPa]	$\nu$	RSS	$R^2$	F	P-value
ST1	2.656	0.231	$1.989 \times 10^{-4}$	0.980	4508.453	$\ll 0.05$
ST2	2.632	0.172	$3.174 \times 10^{-4}$	0.946	2271.625	$\ll 0.05$
ST3	2.491	0.220	$1.274 \times 10^{-4}$	0.991	1894.623	$\ll 0.05$
ST4	2.882	0.172	$3.620 \times 10^{-4}$	0.916	1243.455	$\ll 0.05$
ST5	1.762	0.258	$1.980 \times 10^{-4}$	0.991	11144.462	$\ll 0.05$
ST6	2.975	0.172	$2.105 \times 10^{-4}$	0.952	1894.623	$\ll 0.05$
ST7	1.845	0.237	$4.496 \times 10^{-4}$	0.979	4989.603	$\ll 0.05$
AVG	2.463	-	-	-	-	-
SD	0.434	-	-	-	-	-

significance, thus the method has high accuracy. The fitting results for the splitting tests find the elastic Young modulus between 1.762 GPa and 2.975 GPa with a mean value of 2.463 GPa. The test result of the elastic Young modulus is 2.210 GPa, and the *MPE* (Eq. 17) is 11.46%. Therefore, the fitting method applied to the splitting tests provided a reasonable estimate of the elastic Young modulus simultaneously with the tensile strength determination.

#### 4. Conclusions

The mechanical properties of magnesium-based wood-like material has been evaluated, and following conclusions were drawn:

- (1) In uniaxial compression, the elastic Young modulus was  $2.21 \pm 0.28$  GPa, and Poisson's ratio was  $0.21 \pm 0.03$ . The axial compressive strength was  $8.76 \pm 0.33$  MPa. The splitting tensile strength was  $1.79 \pm 0.12$  MPa. Measurement of the centerline opening displacements showed the deformation in splitting tensile test was consistent with loading by a uniform distributed force.
- (2) During splitting tensile failure, a primary crack initiated from the centre and extended towards the loading ends. Secondary cracks occurred near the loading ends after the primary crack extended across the specimen.
- (3) A new and robust method for identifying crack modes has been proposed and validated. The primary crack of every specimen was mode I, showing that the loading method caused splitting tensile failure and so provided the tensile strength of MWM. Secondary cracks were mainly observed to be mode II or mixed mode I/II cracks, due to shear and tensile-shear failure.
- (4) A method for estimating the elastic Young modulus, simultaneously with the determination of the splitting tensile strength of MWM cubes has been demonstrated by fitting the displacement fields obtained by the DIC to the theoretical displacement curves. Compared with the elastic Young modulus determined by experimental test, the mean percentage error was 11.43%.

#### CRediT authorship contribution statement

**Li Chunjie:** Conceptualization, Formal analysis, Investigation, Methodology, Software, Validation, Visualization, Writing – original draft. **Zhang Huangang:** Funding acquisition, Project administration, Resources, Supervision. **Chen Hongniao:** Conceptualization, Data curation, Formal analysis, Funding acquisition, Project administration, Resources, Supervision, Writing – review & editing. **Marrow T.James:** Funding acquisition, Project administration, Resources, Supervision, Writing – review & editing.

#### Declaration of Competing Interest

The authors declare the following financial interests/personal relationships which may be considered as potential competing interests: Hongniao Chen reports financial support was provided by National Natural Science Foundation of China. Hongniao Chen reports financial support was provided by Guizhou Provincial Natural Science Foundation. Huangang Zhang reports financial support was provided by National Natural Science Foundation of China. James Marrow reports financial support was provided by The Royal Society.

#### Data Availability

Data will be made available on request.

#### Acknowledgement

The work described in this paper was supported by the National Natural Science Foundation of China (52278251, 52068008), Guizhou Provincial Sciences and Technology Projects (ZK[2022] Key 007), and the International Exchanges 2021 funded by the Royal Society (Ref: IEC\NSFC\211449).

## Disclosure Statement

The authors declare that they have no known competing financial interests or personal relationships that could have appeared to influence the work reported in this paper.

## References

- [1] M. Ma, F. Xi, Y. Yin, L. Bing, Contribution of straw disposal to carbon source and sink under the framework of carbon neutrality (in Chinese), *Chin. J. Appl. Ecol.* 33 (05) (2022) 1331–1339, <https://doi.org/10.13287/j.1001-9332.202205.025>.
- [2] J. Wang, S. Wang, Y. Zuo, J. Xiao, Y. Wu, Construction of compatible interface of straw/magnesium oxychloride lightweight composites by coupling agents, *Constr. Build. Mater.* 281 (2021) 122600, <https://doi.org/10.1016/j.conbuildmat.2021.122600>.
- [3] J. Chen, E.M.A. Elbashiry, T. Yu, Y. Ren, Z. Guo, S. Liu, Research progress of wheat straw and rice straw cement-based building materials in China, *Mag. Concr. Res.* 70 (2) (2018) 84–95, <https://doi.org/10.1680/jmacr.17.00064>.
- [4] B. Niu, B.H. Kim, Method for manufacturing corn straw cement-based composite and its physical properties, *Materials* 15 (9) (2022) 3199, <https://doi.org/10.3390/ma15093199>.
- [5] X. Ding, G. Tian, A. Ge, Comparative study on properties of different straw fiber cement composites, *Iop Conf. Ser.: Mater. Sci. Eng.* 479 (2019) 12097, <https://doi.org/10.1088/1757-899x/479/1/012097>.
- [6] J. Yang, H. Zhang, T. Yu, Y. Zheng, K. Sun, Study on the modification mechanism of modifiers on the properties of sawdust-magnesium oxychloride cement composite, *Constr. Build. Mater.* 344 (2022) 128172, <https://doi.org/10.1016/j.conbuildmat.2022.128172>.
- [7] X. Chen, S. Kou, F. Xing, Effect of agriculture and construction wastes on the properties of magnesium oxychloride cement mortar with tourmaline powder, *Materials* 12 (1) (2019) 115, <https://doi.org/10.3390/ma12010115>.
- [8] A.A. Raheem, A.I. Ige, Chemical composition and physicommechanical characteristics of sawdust ash blended cement, *J. Build. Eng.* 21 (2019) 404–408, <https://doi.org/10.1016/j.jobbe.2018.10.014>.
- [9] C. Antwi-Boasiako, L. Ofosuhenne, K.B. Boadu, Suitability of sawdust from three tropical timbers for wood-cement composites, *J. Sustain.* 37 (4) (2018) 414–428, <https://doi.org/10.1080/10549811.2018.1427112>.
- [10] A. Maier, D.L. Manea, Perspective of using magnesium oxychloride cement (MOC) and wood as a composite building material: a bibliometric literature review, *Materials* 15 (5) (2022) 1772, <https://doi.org/10.3390/ma15051772>.
- [11] K. Li, Y. Wang, N. Yao, A. Zhang, Recent progress of magnesium oxychloride cement: manufacture, curing, structure and performance, *Constr. Build. Mater.* 255 (2020) 119381, <https://doi.org/10.1016/j.conbuildmat.2020.119381>.
- [12] Y. Guo, Y. Zhang, K. Soe, M. Pulham, Recent development in magnesium oxychloride cement, *Struct. Concr.* 19 (5) (2018) 1290–1300, <https://doi.org/10.1002/suco.201800077>.
- [13] F. Wang, X. Xu, B. Zhou, S. Zhong, Preparation of straw-magnesium oxychloride cement composites (in Chinese), *J. Build. Mater.* 22 (01) (2019) 135–141, <https://doi.org/10.3969/j.issn.1007-9629.2019.01.020>.
- [14] J.V.F. Silva, N.A. Bianchi, C.A.B. Oliveira, J.C. Caraschi, Characterization of composite formed by cement and wheat straw treated with sodium hydroxide, *Bioresources* 14 (2) (2019) 2472–2479, <https://doi.org/10.15376/biores.14.2.2472-2479>.
- [15] X. Zhou, Z. Li, Light-weight wood-magnesium oxychloride cement composite building products made by extrusion, *Constr. Build. Mater.* 27 (1) (2012) 382–389, <https://doi.org/10.1016/j.conbuildmat.2011.07.033>.
- [16] X. Zhang, H. Zhang, H. Liu, Q. Wu, Experimental study on compressive strength of wood like materials (in Chinese), *China Water Transp.* 21 (01) (2021) 148–150.
- [17] H. He, H. Zhang, J. Yang, Z. Fan, W. Chen, Effect of pressing pressure on the mechanical properties and water resistance of straw/sawdust-magnesium oxychloride cement composite, *Constr. Build. Mater.* 383 (2023) 131362, <https://doi.org/10.1016/j.conbuildmat.2023.131362>.
- [18] J. Yang, H. Zhang, T. Yu, K. Sun, Y. Zheng, Constitutive relationships and acoustic emission behavior of plant-fiber/magnesium oxychloride cement composites under uniaxial compressive load, *Constr. Build. Mater.* 404 (2023) 133194, <https://doi.org/10.1016/j.conbuildmat.2023.133194>.
- [19] Y. Liu, H. Zhang, Q. Wu, H. Liu, Preliminary experimental investigation on mechanical properties of similar wood material (in Chinese), *J. Guizhou Univ. Nat. Sci.* 35 (04) (2018) 106–112, <https://doi.org/10.15958/j.cnki.gdxbzrb.2018.04.20>.
- [20] H. Haeri, V. Sarfarazi, Z. Zhu, Analysis of crack coalescence in concrete using neural networks, *Strength Mater.* 48 (6) (2016) 850–861, <https://doi.org/10.1007/s11223-017-9831-2>.
- [21] J. Fu, H. Haeri, M.D. Yavari, V. Sarfarazi, M.F. Marji, Effects of the measured noise on the failure mechanism of pre-cracked concrete specimens under the loading modes I, II, III, and IV, *Strength Mater.* 53 (6) (2021) 938–949, <https://doi.org/10.1007/s11223-022-00362-x>.
- [22] J.W. Fu, H. Haeri, V. Sarfarazi, A.H. Noshadi, M.F. Marji, M.D. Guo, Investigating the failure behavior of gypsum specimens with non-persistent vertical notch under uniaxial compression, *Strength Mater.* 54 (1) (2022) 14–32, <https://doi.org/10.1007/s11223-022-00374-7>.
- [23] H. Ren, Y. Du, S. Song, Deformation and failure of concrete splitting based on DIC method (in Chinese), *Chin. J. High Press. Phys.* 36 (04) (2022) 91–100, <https://doi.org/10.11858/gwylxb.20220509>.
- [24] J.D. Davies, D.K. Bose, Stress distribution in splitting tests, *Acids J. Proc.* 65 (8) (1968) 662–669, <https://doi.org/10.14359/7504>.
- [25] L. Małyszko, E. Kowalska, P. Bilko, Splitting tensile behavior of autoclaved aerated concrete: Comparison of different specimens' results, *Constr. Build. Mater.* 157 (2017) 1190–1198, <https://doi.org/10.1016/j.conbuildmat.2017.09.167>.
- [26] H. Chen, D. Liu, Fracture and damage properties of high-strength concrete under cyclic loading, *Constr. Build. Mater.* 360 (2022) 129494, <https://doi.org/10.1016/j.conbuildmat.2022.129494>.
- [27] H. Chen, D. Liu, Fracture process zone of high-strength concrete under monotonic and cyclic loading, *Eng. Fract. Mech.* 277 (2023) 108973, <https://doi.org/10.1016/j.engfractmech.2022.108973>.
- [28] A. Fallah Pour, G.D. Nguyen, T. Vincent, T. Ozbakkaloglu, Investigation of the compressive behavior and failure modes of unconfined and FRP-confined concrete using digital image correlation, *Compos. Struct.* 252 (2020) 112642, <https://doi.org/10.1016/j.compstruct.2020.112642>.
- [29] L. Liu, H. Li, X. Li, D. Wu, G. Zhang, Underlying mechanisms of crack initiation for granitic rocks containing a single pre-existing flaw: insights from digital image correlation (DIC) analysis, *Rock Mech. Rock Eng.* 54 (2) (2021) 857–873, <https://doi.org/10.1007/s00603-020-02286-x>.
- [30] GB/T 50081–2019, "Standard for test methods of concrete physical and mechanical properties." (2019).
- [31] S. Bhowmik, S. Ray, An experimental approach for characterization of fracture process zone in concrete, *Eng. Fract. Mech.* 211 (2019) 401–419, <https://doi.org/10.1016/j.engfractmech.2019.02.026>.
- [32] V.P. Rajan, M.N. Rossol, F.W. Zok, Optimization of digital image correlation for high-resolution strain mapping of ceramic composites, *Exp. Mech.* 52 (9) (2012) 1407–1421, <https://doi.org/10.1007/s11340-012-9617-1>.
- [33] Y. Xu, H. Chen, Y. Tang, Study on fracture parameters and fracture process zone of manufactured-sand recycled aggregate concrete, *Constr. Build. Mater.* 361 (2022) 129613, <https://doi.org/10.1016/j.conbuildmat.2022.129613>.
- [34] N. Erarslan, D.J. Williams, Experimental, numerical and analytical studies on tensile strength of rocks, *Int. J. Rock Mech. Min. Sci.* 49 (2012) 21–30, <https://doi.org/10.1016/j.ijrmms.2011.11.007>.
- [35] N.I. Muskhelishvili, Some basic problems of the mathematical theory of elasticity, Noordhoff Groningen, 1953.
- [36] J. Qu, The experimental study on the split strength of SFRC, PhD Thesis, Harbin Engineering University, Harbin, 2010.
- [37] A.A. Griffith, The phenomenon of rupture and flow in solids, *philosophical transactions of the royal society of London Ser. a, Contain. Pap. a Math. Or. Phys. Character* 221 1995 163 198 doi: 10.1098/rsta.1921.0006.



- [38] J. Cheng, Analytical solution and numerical simulation of the splitting tensile strength of cubic brittle materials, MSE Thesis, Southeast University, Nanjing, 2021.
- [39] D. Liu, T. Zillhardt, P. Earp, S. Kabra, T. Connolley, T. James Marrow, In situ measurement of elastic and total strains during ambient and high temperature deformation of a polygranular graphite, *Carbon* 163 (2020) 308–323, <https://doi.org/10.1016/j.carbon.2020.03.020>.
- [40] S.Y. Alam, P. Kotronis, A. Loukili, Crack propagation and size effect in concrete using a non-local damage model, *Eng. Fract. Mech.* 109 (2013) 246–261.
- [41] J. Marrow, D. Scotson, A. Koko, X. Jin, H. Chen, Y. Chen, P. Earp, H. Wu, Small-Specimen Testing, with Image-Based Analysis, for Crack Propagation Resistance in Polygranular Nuclear Graphite, 2022, pp. 1–17.
- [42] J.W. Fu, M.D. Guo, H. Haeri, V. Sarfarazi, M.F. Marji, A discrete element analysis of the indirect tensile failure in hollow Brazilian discs of bedded geo-materials, *Strength Mater.* 54 (3) (2022) 462–472, <https://doi.org/10.1007/s11223-022-00421-3>.
- [43] Y. Choi, R.L. Yuan, Experimental relationship between splitting tensile strength and compressive strength of GFRC and PFRC, *Cem. Concr. Res.* 35 (8) (2005) 1587–1591, <https://doi.org/10.1016/j.cemconres.2004.09.010>.
- [44] W. Zhong, J. Pan, J. Wang, C. Zhang, Size effect in dynamic splitting tensile strength of concrete: Experimental investigation, *Constr. Build. Mater.* 270 (2021) 121449, <https://doi.org/10.1016/j.conbuildmat.2020.121449>.
- [45] S. Carmona, R. Gettu, A. Aguado, Study of the Post-Peak Behavior of Concrete in the Splitting-Tension Test, in: International conference; 3rd, Fracture mechanics of concrete structures; Fracture mechanics of concrete structures; FRACTURE MECHANICS OF CONCRETE STRUCTURES, Freiburg, Gifu, Japan, 1998, pp. 111–120.
- [46] Q. Wang, L.J. Sun, D.C. Wang, J.W. Fu, C.L. Guo, H. Haeri, Particle flow modeling for the crack growth analysis of non-persistent cracks, *Strength Mater.* 55 (2) (2023) 371–383, <https://doi.org/10.1007/s11223-023-00531-6>.
- [47] K. Wang, D.C. Jansen, S.P. Shah, A.F. Karr, Permeability study of cracked concrete, *Cem. Concr. Res.* 27 (3) (1997) 381–393, [https://doi.org/10.1016/S0008-8846\(97\)00031-8](https://doi.org/10.1016/S0008-8846(97)00031-8).
- [48] L. Han, Y. He, H. Zhang, Study of rock splitting failure based on Griffith strength theory, *Int. J. Rock Mech. Min. Sci.* 83 (2016) 116–121, <https://doi.org/10.1016/j.ijrmms.2015.12.011>.
- [49] K.B. Broberg, Differences Between Mode I and Mode II Crack Propagation, *Pure Appl. Geophys.* 163 (9) (2006) 1867–1879, <https://doi.org/10.1007/s00024-006-0101-7>.
- [50] L. Zhou, V. Sarfarazi, H. Haeri, P. Ebneabbasi, M. Fatehi Marji, M. Hassannezhad Vayani, A new approach for measurement of the fracture toughness using the edge cracked semi-cylinder disk (ECSD) concrete specimens, *Mech. Based Des. Struct. Mech.* 51 (5) (2023) 2896–2917, <https://doi.org/10.1080/15397734.2021.1911667>.
- [51] A. Bobet, H.H. Einstein, Fracture coalescence in rock-type materials under uniaxial and biaxial compression, *Int. J. Rock. Mech. Min. Sci.* 35 (7) (1998) 863–888, [https://doi.org/10.1016/S0148-9062\(98\)00005-9](https://doi.org/10.1016/S0148-9062(98)00005-9).
- [52] C.H. Park, A. Bobet, Crack coalescence in specimens with open and closed flaws: a comparison, *Int. J. Rock Mech. Min. Sci.* 46 (5) (2009) 819–829, <https://doi.org/10.1016/j.ijrmms.2009.02.006>.
- [53] L.N.Y. Wong, H.H. Einstein, Crack coalescence in molded gypsum and carrara marble: Part 1. Macroscopic observations and interpretation, *Rock Mech. Rock Eng.* 42 (3) (2009) 475–511, <https://doi.org/10.1007/s00603-008-0002-4>.
- [54] H. Haeri, V. Sarfarazi, P. Ebneabbasi, M.R.M. Aliha, G. Saeedi, H.R. Karimi, A.M. Far, Edge notched disc test for evaluation of mode-I fracture toughness of brittle material, *J. Mater. Res. Technol.* 27 (2023) 4997–5009, <https://doi.org/10.1016/j.jmrt.2023.10.322>.
- [55] T.J. Pirzada, D. Liu, J. Ell, H. Barnard, I. Šulák, M. Galano, T.J. Marrow, R.O. Ritchie, In situ observation of the deformation and fracture of an alumina-alumina ceramic-matrix composite at elevated temperature using x-ray computed tomography, *J. Eur. Ceram. Soc.* 41 (7) (2021) 4217–4230, <https://doi.org/10.1016/j.jeurceramsoc.2021.01.030>.
- [56] A. Koko, P. Earp, T. Wigger, J. Tong, T.J. Marrow, J-integral analysis: An EDXD and DIC comparative study for a fatigue crack, *Int. J. Fatigue* 134 (2020) 105474, <https://doi.org/10.1016/j.ijfatigue.2020.105474>.
- [57] X. Jin, T.J. Marrow, J. Wang, Y. Chen, H. Chen, D. Scotson, B. Wang, H. Wu, X. Fan, Crack propagation in fine grained graphites under mode I and mixed-mode loading, as observed in situ by microtomography, *Carbon* 193 (2022) 356–367, <https://doi.org/10.1016/j.carbon.2022.03.051>.
- [58] X. Su, W. Wan, F.P.E. Dunne, T.J. Marrow, Crack field analysis by optical DIC of short cracks in Zircaloy-4, *Procedia Struct. Integr.* 39 (2022) 663–670, <https://doi.org/10.1016/j.prostr.2022.03.139>.
- [59] M.R. Joyce, T.J. Marrow, Microstructural scale strain localisation in nuclear graphite, *J. Nucl. Mater.* 381 (1-2) (2008) 171–176, <https://doi.org/10.1016/j.jnucmat.2008.07.013>.
- [60] S. Jemioło, E. Szmigiera, P. Łukowski, Determining of elastic constants and tensile strength of brittle materials in Brazilian test, *Warsaw University of Technology Publishing House*, 2015, pp. 81–92.
- [61] G. Zhou, J. Si, Advanced neural-network training algorithm with reduced complexity based on Jacobian deficiency, *IEEE Trans. Neural Netw.* 9 (3) (1998) 448–453, <https://doi.org/10.1109/72.668886>.